Research

Author for correspondence:
Thomas Meersmann
e-mail: thomas.meersmann@nottingham.ac.uk

†Present address: Clinical Research Imaging Centre, Queen's Medical Research Institute, Little France Crescent, University of Edinburgh, Edinburgh EH16 4TJ, UK.
‡Present address: Carestream Health Inc., 8124 Pacific Avenue, White City, OR 97503, USA.

Hyperpolarized 83Kr magnetic resonance imaging of alveolar degradation in a rat model of emphysema

David M. L. Lilburn[1,†], Clémentine Lesbats[1], Joseph S. Six[1,‡], Eric Dubuis[2], Liang Yew-Booth[2], Dominick E. Shaw[3], Maria G. Belvisi[2], Mark A. Birrell[2], Galina E. Pavlovskaya[1] and Thomas Meersmann[1]

[1]Sir Peter Mansfield Imaging Centre, Division for Respiratory Medicine, School of Medicine, University of Nottingham, Nottingham NG7 2RD, UK
[2]Respiratory Pharmacology, Pharmacology and Toxicology, Faculty of Medicine, National Heart and Lung Institute, Imperial College London, London SW7 2AZ, UK
[3]City Hospital Nottingham, Nottingham Respiratory Research Unit, Nottingham NG5 1PB, UK

Hyperpolarized 83Kr surface quadrupolar relaxation (SQUARE) generates MRI contrast that was previously shown to correlate with surface-to-volume ratios in porous model surface systems. The underlying physics of SQUARE contrast is conceptually different from any other current MRI methodology as the method uses the nuclear electric properties of the spin $I = 9/2$ isotope 83Kr. To explore the usage of this non-radioactive isotope for pulmonary pathophysiology, MRI SQUARE contrast was acquired in excised rat lungs obtained from an elastase-induced model of emphysema. A significant 83Kr T_1 relaxation time increase in the SQUARE contrast was found in the elastase-treated lungs compared with the baseline data from control lungs. The SQUARE contrast suggests a reduction in pulmonary surface-to-volume ratio in the emphysema model that was validated by histology. The finding supports usage of 83Kr SQUARE as a new biomarker for surface-to-volume ratio changes in emphysema.

1. Introduction

Hyperpolarized krypton-83 (hp 83Kr) enables MRI contrast that is indicative of surface composition [1,2] and the surface-to-volume ratio (S/V) [3] in porous media. The T_1-weighted MRI contrast is generated through surface quadrupolar relaxation (SQUARE) that causes S/V-dependent reduction in the hp 83Kr MR signal intensity as sketched in figure 1. Pulmonary SQUARE MRI contrast between major pulmonary airways and the alveolar regions has recently been demonstrated in excised rat lungs [4]. In this publication, the potential of hp 83Kr SQUARE contrast for lung pathophysiology is evaluated using *ex vivo* MRI of an established rat model of emphysema. The emphysema model was selected for this proof of concept study because of the well-known deterioration of the alveolar surface that is expected to cause increased SQUARE T_1 times. Following the MRI acquisition, the alveolar surface deterioration can be quantified through histology.

Emphysema is a component of chronic obstructive pulmonary disease (COPD), the fourth leading cause of death worldwide [5]. The development of emphysema is mainly linked to cigarette smoking with a smaller proportion attributed to pollution, occupational exposure or intrinsic factors [6]. Over time, there is significant alveolar destruction with the resulting reduction in surface area for gas exchange with an accompanied loss of lung elasticity. Unfortunately, current routine investigations such as lung function tests often fail to diagnose the disease until the later stages [7] once a significant amount of damage has been done. There is therefore a need for new biomarkers to detect the disease in the early stages and to help separate COPD phenotypes [8].
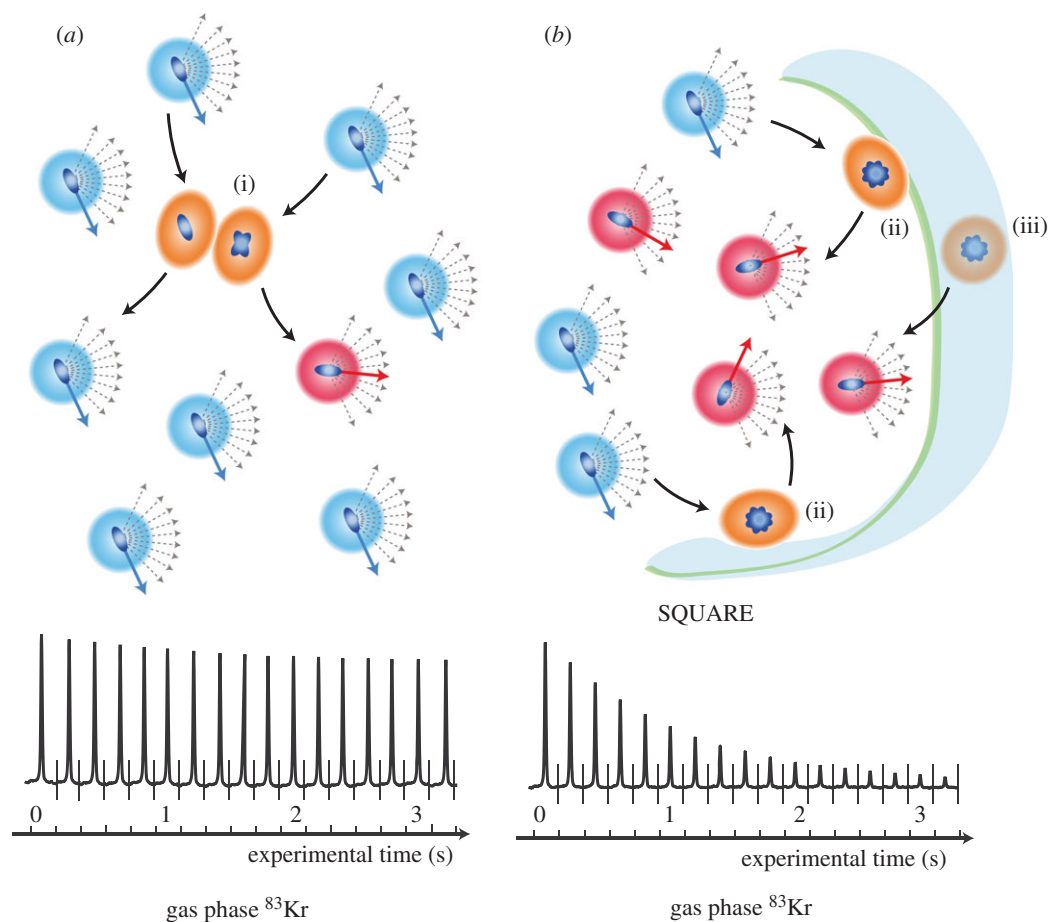
Figure 1. Illustration of the concept of hp ^{83}Kr SQUARE contrast. The ^{83}Kr atoms are depicted with the 10 possible spin states of this nuclear spin $I = 9/2$ isotope and with a non-spherical nucleus that possesses a nuclear electric quadrupolar moment. Hyperpolarized ^{83}Kr atoms, drawn in blue, are depicted as occupying the lowest spin state (i.e. corresponding to the highest MRI signal intensity). However, longitudinal T_1 relaxation will cause the spins to assume other states (atoms indicated in red), thus reducing the MRI signal intensity. Quadrupolar relaxation occurs when the electron cloud of ^{83}Kr is forced out of the spherical shape. (a) In the bulk gas phase a non-spherical symmetry is caused by collisions (i) leading to the gas phase signal decay within minutes. (b) When surfaces are present, surface adsorption (ii) and possibly dissolution into deeper surface regions (iii) will lead to surface quadrupolar relaxation (SQUARE). Rapid exchange causes transfer of the SQUARE effect into the gas phase where the rapid signal decay is observed with typical T_1 times approximately 1 s in rat lungs. See Material and methods section for further details.

Investigations of COPD and emphysema, in particular, have developed over the past decade with human studies using both computed tomography (CT) [9] and magnetic resonance imaging (MRI)-based techniques [10,11]. Hyperpolarized noble gas MRI [12–14] using ^{3}He and ^{129}Xe is able to provide measurements of ventilation and is able to delineate poorly ventilated and non-functioning lung regions [11,12]. Recently, visualization of delayed collateral ventilation into lung regions has been performed [15], providing information complementary to CT-based techniques. Furthermore, hp ^{3}He and hp ^{129}Xe provide measurements of the lung microstructure through the apparent diffusion coefficient (ADC) [16–24]. Using animal models of emphysema, the distinction between healthy and emphysematous tissue was possible through fractional ventilation generated hp ^{3}He MRI contrast before an increase in alveolar diameter could be determined through histology [25,26]. Unlike fractional ventilation that is decreased in the disease model, ADC was found to be increased in long-term disease models developed over a six-month period [21]. A very promising new pulmonary MRI contrast can be obtained by probing the dissolved phase of hp ^{129}Xe. A host of innovative new techniques, such as xenon polarization transfer contrast (XTC) [23,27–30], xenon alveolar capillary transfer (XACT) [31] and chemical shift saturation recovery spectroscopy (CSSR) [29,32,33] enable selective detection of gas phase xenon, tissue

and plasma (TP) dissolved xenon and xenon interacting with red blood cells (RBC). For example, Dregely et al. [23] found a strong correlation between the XTC-based parameter (MXTC-F) and CT data. Using CSSR spectroscopy, Patz et al. [33] found a dramatic decrease in S/V in emphysema patients, while alveolar septal thickness and capillary transit time was not affected. In general, the findings suggest that a sensitive probe for S/V changes is the key to early emphysema diagnosis.

This work sets forth the verification of a new type of hyperpolarized noble gas modality for pulmonary studies, i.e. hp ^{83}Kr SQUARE MRI contrast [4], which may provide a significant addition to existing methodology. Previous work exploring the underlying conceptual physics found SQUARE to be the dominant cause of ^{83}Kr T_1 relaxation observed in the gas phase in high S/V porous media such as lungs. See figure 1 and Material and methods section for an explanation of the SQUARE concept. The purpose of this work is to determine whether the SQUARE effect is sensitive enough to serve as a probe for disease-related lung physiological changes.

The potential significance of SQUARE MRI contrast is that it may enable a novel type of biomarker for pulmonary pathophysiology through a fundamentally different physical effect compared with those used in other pulmonary diagnostic techniques such as hp ^{3}He ADC and hp ^{129}Xe dissolved phase measurements. For example, the associated timescale

of the 'surface probing' is 1–2 orders of magnitude longer than that of ADC measurements. The nature of the contrast generation may provide a methodology sensitive not only to S/V but also to the chemical composition of the surface. Furthermore, in model surfaces quadrupolar noble gas (i.e. ^{131}Xe) relaxation was affected by microscopic surface fine structure [34,35]. Similarly, ^{83}Kr SQUARE is likely to be sensitive to surface corrugation and may, therefore, provide different S/V values compared with dissolved xenon-based techniques [33].

Informed by the surface studies of previous models [1–3,36,37], the underlying hypothesis of this publication is that hp ^{83}Kr SQUARE MRI contrast can serve as a biomarker for the alveolar S/V reduction caused by emphysema. Confirmation of the S/V hypothesis in a preclinical small animal model is a crucial milestone for the development of hp ^{83}Kr MRI. The intratracheal elastase exposure of rat lungs to porcine pancreatic elastase (PPE) generates an established model of emphysema whereby initial inflammation is produced with the subsequent development of airspace enlargement and destruction [38–41]. The experimentally and regulatory less demanding *ex vivo* set-up [14,42] was used for the MRI measurements in this proof of concept work to set the basis for future *in vivo* preclinical and clinical studies.

2. Material and methods

2.1. SQUARE contrast

Figure 1 illustrates the mechanism of SQUARE with the nuclear spin $I = 9/2$ isotope ^{83}Kr. Atomic nuclei are positively charged electric monopoles, however, the nucleus of any spin $I > 1/2$ isotopes is non-spherical leading to a non-uniform nuclear electric charge distribution. The resulting nuclear electric quadrupole moment can interact with the surrounding electrons if the noble gas atom is 'distorted'—i.e. if the electronic cloud assumes a non-spherical symmetry. In the bulk gas phase, far away from surfaces (figure 1a), collisions events with other atoms cause rapidly fluctuating electron cloud distortions that results in ^{83}Kr quadrupolar relaxation with T_1 times of several minutes at ambient pressure. SQUARE (figure 1b) occurs when surface adsorption and possibly dissolution into deeper surface regions takes place. SQUARE can typically not be observed directly owing to strong line broadening and the limited number of atoms at the surface at any given time. However, the SQUARE effect is transferred into the gas phase through rapid exchange and, depending on the S/V ratio, can tremendously accelerate the decay of the hp gas phase signal. SQUARE contrast is, therefore, potentially sensitive to S/V, surface composition and surface temperature. SQUARE caused by high S/V alveolar region of rat lungs reduces the gas phase T_1 time to approximately 1 s leading to the rapid hp ^{83}Kr signal decay in the series of small flip angle spectra in figure 1b.

2.2. ^{83}Kr Spin exchange optical pumping, compression and transfer

Hyperpolarized ^{83}Kr was produced in batch mode by SEOP as described previously described in detail [43]. All MRI was performed using enriched ^{83}Kr (99.925% ^{83}Kr, CHEMGAS, Boulogne, France) to improve the available signal intensity. A 15% krypton 85% N_2 (99.999% purity, Air Liquide, Coleshill, UK) mixture was used to reduce the consumption of expensive isotopically enriched ^{83}Kr. SEOP build-up times of 12 min, corresponding to greater than 92% of the steady-state polarization

were used to reduce the experimental duration. The hyperpolarized gas extraction unit described previously [4,44] was used to allow for below ambient pressure SEOP [4,43] performed at 55–65 kPa [43]. Overall, the method produced a ^{83}Kr nuclear spin polarization of $P = 16$–17% after accounting for depolarization occurring in the gas extraction process [44]. An approximate volume of 12–16 ml of the hp gas mixture (1 : 6.7 Kr:N_2) was obtained for lung imaging every 12 min. Since no viable method currently exist to separate hp ^{83}Kr from the mixture, it is instructional to report the apparent spin polarization of approximately $P_{app} = 2.5\%$. The apparent polarization is the nuclear spin polarization P times the fraction of krypton in the hp gas mixture [43]. A discussion of the nuclear spin polarization P for isotopes with nuclear spin $I > 1/2$ can be found in [45].

2.3. Hyperpolarized gas inhalation

The lungs were suspended in a 5% glucose solution (weight/volume) in the ventilation chamber as described in previous work [14,42]. The chamber was then placed in the centre of the superconducting magnet bore with the temperature kept constant at 295 K throughout the experiments. Active inflation of the lung was accomplished by pulling to a ventilation syringe volume (V_s) of 8 ml. Corresponding inhaled volumes (V_i) were measured separately using the water displacement technique on gas exhalation [14] and are shown in table 1. To limit gas trapping (particularly notable in the PPE-treated lungs) the *ex vivo* lungs were deflated over 30–60 s from $V_s = 8$ ml to maximum exhalation ($V_s = 0$ ml) as has been reported elsewhere [46,47] before hp ^{83}Kr inhalation.

2.4. Magnetic resonance imaging protocol

MRI experiments were performed using a vertical bore 9.4 T Bruker Avance III microimaging system (Bruker Corporation, Billerica, MA, USA) with a standard Bruker double saddle coil tuned to ^{83}Kr resonance frequency of 15.40 MHz. The internal diameter (ID) of the coil was 30 mm.

Coronal images were acquired into 64×32 matrices using a variable flip angle (VFA) FLASH protocol (TE = 1.8 ms, TR = 12.6 ms) [48]. Rectangular RF pulses of constant duration of 0.3 ms and variable power levels were used in all experiments. The imaging protocol had a total acquisition time 0.405 s to minimize the effects of unwanted T_1 decay during acquisition. To obtain T_1-weighted images [4], each imaging sequence was started after a programmed time delay, τ_d, post inhalation. Typically, $\tau_d = 0.2$ s, 0.7 s, 1.2 s, 1.7 s and 2.2 s were used, although some of the T_1 maps were calculated from a series of four images with $\tau_d = 0.5$ s, 1.0 s, 1.5 s and 2.0 s. The inhalation itself was accomplished manually by reducing the pressure in the artificial pleural cavity using the ventilation syringe [14,42]. Slight alternations in the timing of the manual inhalation procedure (approx. ± 0.2 s) were deemed acceptable. In all imaging experiments each individual image was acquired from a single inhalation cycle using one VFA FLASH acquisition and no signal averaging. The resulting FOV was 50.9×40.7 mm^2.

2.5. Image reconstruction and T_1 analysis

The raw 32×32 datasets were apodized using sine-bell squared function and zero filled to 64 points in each spatial domain before Fourier transformation. Final image resolution was 0.795×0.635 mm^2 in the frequency encoding (longitudinal) and in the phase encoding (transverse) directions, respectively. These final 64×64 magnitude images were exported to IGOR Pro (v. 6.01, Wavemetrics, Lake Oswego, OR, USA) for T_1 analysis.

The T_1 datasets were created for each series of images by combining the images acquired at the individual time delays τ_d into a three-dimensional dataset where the first image in

Table 1. Demographic data from satellite subjects (histology only) and those used for hp ^{83}Kr imaging (with subsequent histology). Summary of rat weights, whole lung mean alveolar area $\pm$ standard deviation of the mean, inhaled volumes (V_i) $\pm$ standard deviation corresponding to inflation (syringe) volume $V_s = 8$ ml with associated inhalation pressures $\pm$ standard deviation. No values for V_i were determined in the histology groups. Values omitted were not measured.

	identifier	rat weight (g)	whole lung MAA (10^4 μm^2)	lung usage MRI: hp ^{83}Kr MRI including histology, Histology: (satellite group)	inhaled volume in MRI, V_i (ml)
control	CL.1	492	—	MRI	7.0 ± 0.3
	CL.2	555	2.5 ± 0.1	MRI	6.8 ± 0.1
	CL.3	499	3.7 ± 0.6	MRI	6.8 ± 0.1
	CL.4	400	1.9 ± 0.1	histology	N/A
	CL.5	412	2.5 ± 0.4	histology	N/A
elastase (PPE) treated	EL.1	390	6.3 ± 1.1	MRI	5.9 ± 0.7
	EL.2	508	6.8 ± 1.1	MRI	6.1 ± 0.6
	EL.3	416	5.1 ± 1.0	MRI	6.9 ± 0.3
	EL.4	440	4.5 ± 0.6	MRI	7.3 ± 0.4
	EL.5	513	3.6 ± 1.0	MRI	6.1 ± 0.2
	EL.6	382	4.8 ± 1.4	histology	N/A
	EL.7	436	10.8 ± 6.2	histology	N/A

the set corresponded to the image acquired at the smallest time delay, τ_d as described in [4]. The T_1 values outside of the 0 s $< T_1 \leq 6$ s range were rejected as physically not meaningful. The T_1 values within the range of 0 s $< T_1 \leq 6$ s but located outside the lung contour region, or the region of interest (ROI), were also discarded. The ROI was determined from the first image in each T_1 set. These final T_1 maps were used to produce T_1 histograms for each lung reported in this study.

The T_1 data collected from the ROI in each T_1 map were binned into 200 intervals with 0.03 s increment. The resulting histograms were analysed using build-in Multipeak 1.4 fitting procedure and automated peak picking. A bi-modal Gaussian distribution of T_1 values in the lung was assumed because of the distinct alveolar and conducting airway compartments present in the lung. The results of the analysis returned the most probable (expected value, EV) relaxation time, T_1^{EV}, its probability and distribution measured as full width, half maximum, FWHM(T_1) for each of the two Gaussian components.

2.6. Model characterization: the elastase model and preparation for ex vivo MRI

Male Sprague-Dawley rats (260–300 g) were purchased from Harlan UK Ltd. (Bicester, UK). Home Office guidelines for animal welfare based on the Animals (Scientific Procedures) Act 1986 were strictly observed. Experimental emphysema was induced by instilling one dose of 120 U kg^{-1} PPE (Merck Chemicals Ltd, Nottingham, UK) intratracheally at 1 ml kg^{-1} directly into the airways under general anaesthesia (inhaled isoflurane 4% with medical grade oxygen for 3–4 min) [40,49]. Control animals were similarly treated with 1 ml kg^{-1} sterile saline (Fresenius Kabi Ltd, Manor Park, UK) at the same time. At 28 days after intratracheal dosing animals were weighed and euthanized by overdose of sodium pentobarbital 200 mg kg^{-1} intra-peritoneal (Merial Animal Health, Harlow, UK). After confirmation of death, a catheter was inserted into the caudal vena cava to allow flushing of the pulmonary circulation with 20 ml heparin 100 IU ml^{-1} (Wockhardt UK Ltd, Wrexham, UK) in 0.9% saline solution (Baxter Healthcare Ltd, Thetford, UK)

followed by 20 ml^{-1} Dublecco's phosphate buffer solution (D-PBS, Sigma-Aldrich Ltd, Gillingham, UK) to remove residual blood from the pulmonary circulation. The heart and lungs were subsequently removed en masse.

Lungs for ex vivo hp ^{83}Kr imaging had a polytetrafluoroethylene (PTFE) adapter tube inserted into the trachea 5–10 mm above the carina and sutured into place. The heart and lungs were then suspended in 5% glucose solution (weight/volume) (Baxter Healthcare Ltd, Thetford, UK) with the trachea pointing downwards as has previously reported [14,42]. The ex vivo lungs were repeatedly inflated with 8–10 ml of room air to check for gas leaks either from the suture around the trachea or the lungs themselves. The lungs were chilled to 278 K for transportation to the imaging facility during which time they were repeatedly inflated with 8–10 ml of air at 30–60 min intervals. Time from lung harvest to the start of imaging was no more than 8 h for each lung.

2.7. Model characterization: alveolar cross-section measurements

PPE-induced changes in air space were measured in both a satellite group of rats and on the ex vivo lungs used for hp ^{83}Kr MRI. Lungs from both groups were similarly prepared by inflating to forced vital capacity (25 cm H$_2$O) with 5% formalin–saline solution (Sigma-Aldrich Ltd, Gillingham, UK). The trachea was then tied off and the lungs and heart removed en bloc and placed in formalin. After at least 24 h in formalin, an experienced histologist processed the lungs. Sections were cut from the wax embedded samples using a microtome and stained with H&E.

Experimental emphysema was assessed by measuring average air space area using a method describe by Belloni et al. [50] and used previously [40]. Briefly, computer-assisted image analysis was performed using an Olympus BX40 microscope and Zeiss image-processing software (Imaging Associates, Bicester, UK). Using colour thresholding techniques, the total alveolar air space area and the number of air spaces was measured from five random fields per sample. From these figures the mean air space area was calculated. Any fields
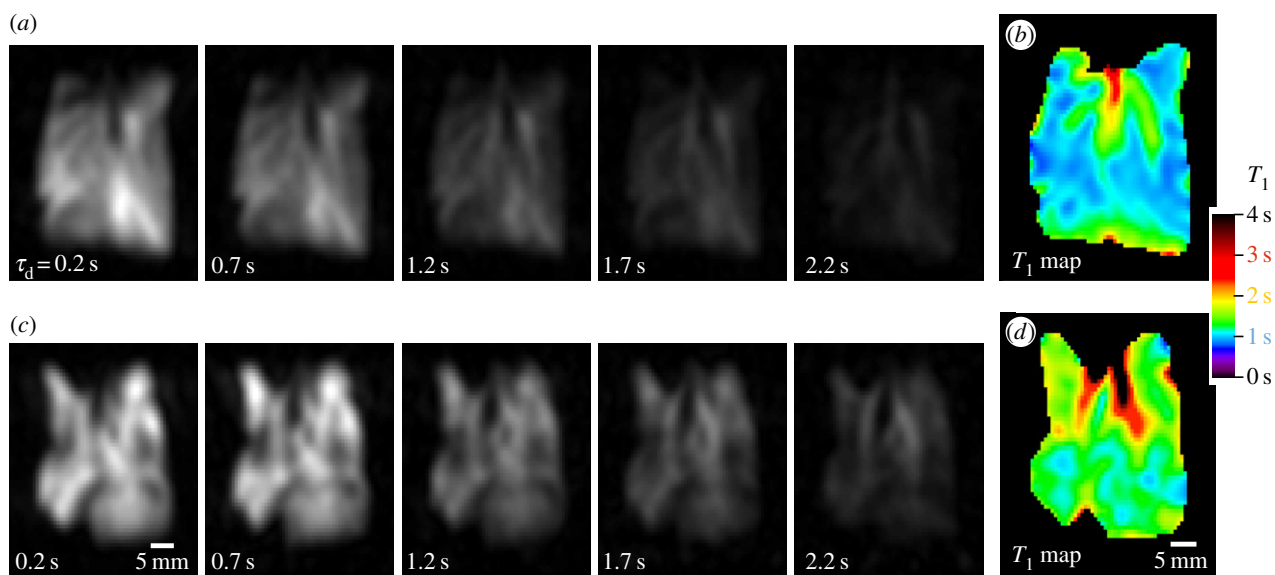
Figure 2. Series of hp ^{83}Kr MR images with resultant T_1 maps in control and PPE-treated lungs. Each image was acquired using a new delivery of hp ^{83}Kr. (a) VFA FLASH MRI with no slice selection in control lung CL.2, using a variable relaxation delay, τ_d, ranging from 0.2 to 2.2 s between hp gas inhalation and acquisition as indicated in the figure. Note that the major airways are less affected than the lung parenchyma by increasing τ_d values. (b) The resultant SQUARE T_1 map for the control lung displays longer T_1 values (green) for the major airways and shorter values for the alveolar region (blue). (c) VFA FLASH MRI as in (a) for the PPE-treated lung EL.1. The lung exhibits heterogeneity in ventilation that is likely caused by the PPE treatment but is not a clear indicator for emphysema. (d) The resultant SQUARE T_1 map of the PPE-treated lung displays prolonged relaxation times (green) in the alveolar area compared with the control SQUARE T_1 map above.

containing airways or vasculature were excluded. The person assessing the slides was blinded to the treatment. Details of control and PPE-treated lungs are shown in table 1 with average measurements of mean alveolar area (MAA) in the satellite group and in those lungs processed post ex vivo hp ^{83}Kr MRI.

3. Results

3.1. Comparison hyperpolarized ^{83}Kr magnetic resonance images and resultant T_1 maps between control and porcine pancreatic elastase-treated groups

Examples of hp ^{83}Kr MR images acquired using the series of increasing delay times, τ_d, and the resultant SQUARE T_1 maps are displayed in figure 2. Compared with the control lungs, a significant heterogeneity of ventilation was found for in the PPE-treated lung. However, heterogeneous ventilation is not particular to emphysema as it can be caused by a variety of diseases and effects. For example, heterogeneous ventilation was also observed in two of the ex vivo control lungs shown in figure 3. Furthermore, ventilation MRI with a better image resolution can be obtained through hp ^{3}He or hp ^{129}Xe and the focus of this work was on T_1 relaxation generated contrast. The hp ^{83}Kr MR images in figure 2a demonstrate how increasing τ_d delay time between inhalation and image acquisition (i.e. from 0.2 s to 2.2 s) leads to a decrease in hp ^{83}Kr signal intensity due to T_1 relaxation. As sketched in figure 1a, the ^{83}Kr gas phase relaxation outside the lung is in the order of minutes [51]. The fast ^{83}Kr T_1 relaxation found within the lung is therefore predominantly caused by interactions of the krypton atoms with the surrounding surface—i.e. by the SQUARE effect. Note 'surface' does not necessarily refer solely to the outermost surfactant layer and deeper levels, including

cell membranes, may contribute as long as fast exchange transfers the depolarized ^{83}Kr back into the alveolar gas phase where MRI signal detection takes place (only gas phase ^{83}Kr signals are MR observable—see also figure 1). In any case however, the ^{83}Kr relaxation time is expected to be sensitive to the S/V ratio and the purpose of this study is to investigate whether SQUARE can serve as an indicator for the emphysema model.

Although other factors, such as chemical composition affect SQUARE [3] the expected strong dependence on S/V ratios is the likely cause for regions with lower S/V, such as the major airways in the control lung, to experience a slower T_1 relaxation and thus a slower depolarization rate. These areas remain 'bright' in the MR images while areas with higher S/V lead to 'dark' regions of faster depolarization. The T_1 map calculated from the delay time τ_d-dependent signal decay leads to the actual SQUARE contrast images shown in figure 2b for the control lung and figure 2d for the elastase-treated lung. Prolonged relaxation times were found for the major airways compared with the alveolar region in the control lung in figure 2b (see also ref. [4]). PPE-treated lungs, serving as a model for emphysema, are imaged for the first time with hp ^{83}Kr in this work. The hp ^{83}Kr SQUARE T_1 map of the lung shown in figure 2d exhibits increased T_1 values for the alveolar region compared with control lungs. This is reflected in the SQUARE T_1 map that displays an elevated level of green colour compared with figure 2b (far right).

Figure 3 depicts the T_1 maps of all three control lungs. The data from the T_1 maps were used for histogram analysis with frequencies of T_1 values within 0.03 s intervals. The T_1 relaxation time distribution of the histograms was analysed using bimodal Gaussian distribution function. The four characteristic T_1 times from this fitting—i.e. the most probable (expected value, EV) relaxation time, T_1^{EV}, of each of the two Gaussian components and their distribution measured as full width, half maximum, FWHM(T_1), are listed in
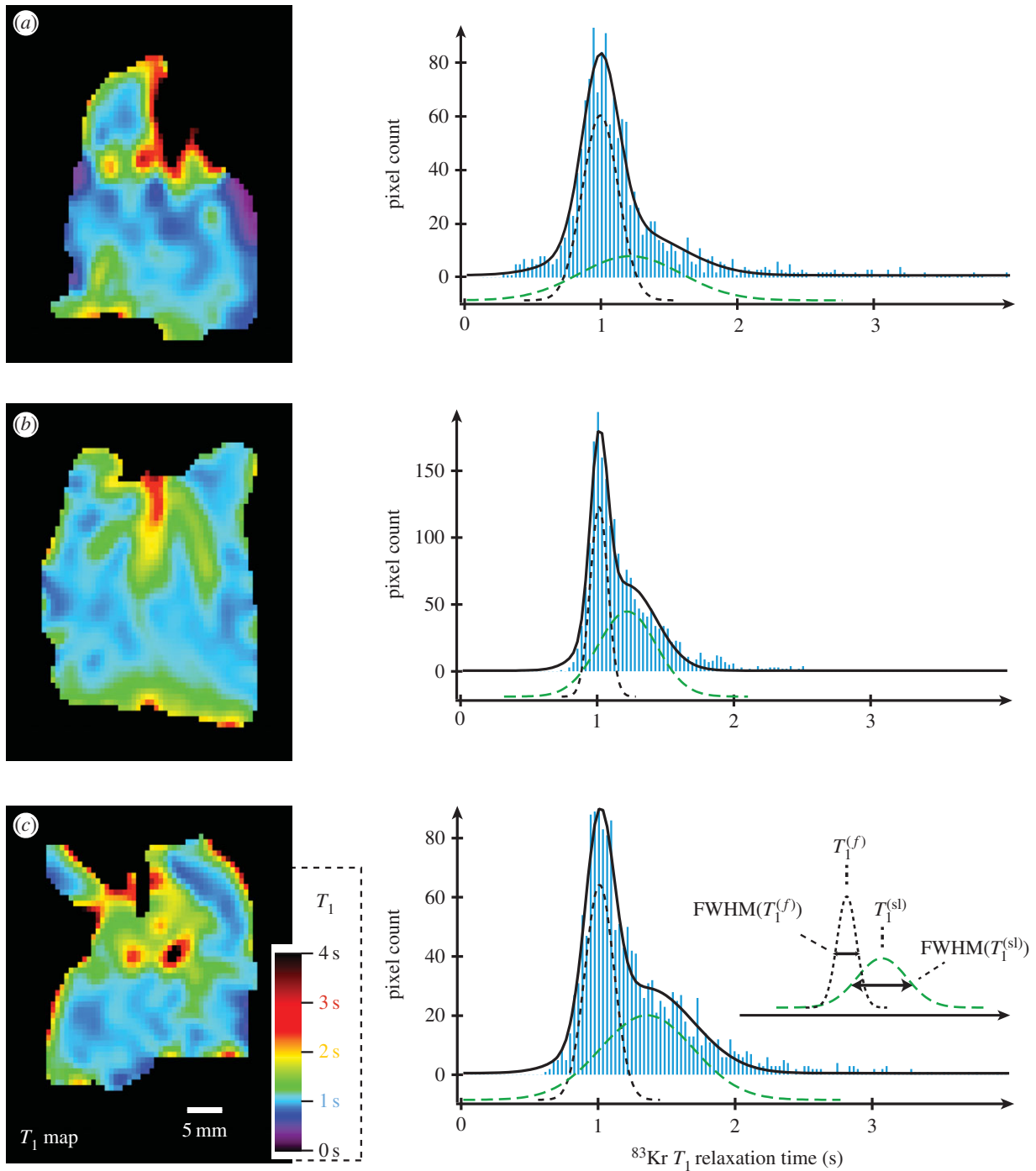
Figure 3. ^{83}Kr MRI T_1 maps (SQUARE contrast) of three control lungs and their corresponding histograms. The SQUARE T_1 maps have been obtained as described in figure 2. Blue colours in the alveolar regions indicate short T_1 values around 1 s. The histograms depict the frequencies (i.e. pixel count from the SQUARE T_1 maps) of T_1 values within 0.03 s intervals. Bimodal fitting leads to a narrow distribution of fast relaxing pixels centred around $T_1^{EV(f)} \approx 1$ s (black dotted line—displayed with negative pixel count offset for clarity) and a broader distribution centred around $T_1^{EV(f)} \approx 1.3$ s (green dashed line -negative pixel count axis offset). The solid black line displays the sum of the two Gaussian distributions. The characteristic T_1 times are explained in insert in histogram (c) and the specific values for each lung and averaged data are listed in table 2 with lung CL.1 shown in (a), CL.2 in (b) and CL.3 in (c).

table 2. The Gaussian distribution of the fast relaxing component centred around $T_1^{EV(f)}$ is indicated by a black dotted line in the histograms, whereas the slow relaxing group, centred around $T_1^{EV(sl)}$, is displayed by the green dashed Gaussian curve. The sum of both components results in the black solid line that very closely resembles the histograms, suggesting that bimodal fitting is a good approach for extraction of parameters that are characteristic for the SQUARE behaviour of a lung.

Figure 4 shows the SQUARE T_1 maps and histograms for PPE-treated lungs. SQUARE T_1 maps and histograms display

marked differences between PPE-treated and control lungs as can also be noted by the characteristic T_1 times from the bimodal fitting listed in table 2. The combined histograms for all three control lungs are shown together with the combined histograms of the four elastase-treated lungs in figure 5.

Figure 6 displays a fifth lung (EL.5) from the PPE group that exhibits SQUARE characteristics very similar to that of control lungs. However, table 1 shows that the averaged MAA is fairly low with MAA = 3.6×10^4 μm and thus is similar to that of the control group. The regional (lobar) MAA values are shown in figure 6c together with the

Table 2. Characteristic T_1 times from bimodal fitting of the histograms of all lungs used in this work.

	rat identifier	$T_1^{EV(f)}$(s) mean	FWHM($T_1^{(f)}$) (s) mean	$T_1^{EV(sl)}$(s) mean	FWHM($T_1^{(sl)}$) (s) mean
control lung	CL.1	0.9958	0.19619	1.2353	0.53927
	CL.2	1.0130	0.091234	1.2189	0.30050
	CL.3	1.0099	0.14987	1.3556	0.48057
average $\pm$ standard deviation		1.00620 ± 0.009	0.14576 ± 0.053	1.2699 ± 0.075	0.44011 ± 0.124
combined histogram of control lungs (figure 5, blue histogram)		1.0112	0.13073	1.2494	0.38797
elastase (PPE) treated lung	EL.1	1.2559	0.12770	1.4787	0.32787
	EL.2	1.2311	0.30498	1.7067	0.52674
	EL.3	1.3697	0.28202	2.0474	0.63887
	EL.4	1.1576	0.21975	1.5708	0.71203
average $\pm$ standard deviation		1.25358 ± 0.088	0.23361 ± 0.079	1.7009 ± 0.249	0.55138 ± 0.167
combined histogram of elastase (PPE) treated lungs (figure 5, red histogram)		1.2734	0.28201	1.7288	0.54928
	EL.5	0.94994	0.1333	1.2257	0.4500

averaged MAA values from the control and elastase groups. All lobes except for the left lung lobe of the lung display values in line with the control group. The left lung lobe exhibits increased MAA significantly above the average from the PPE group.

4. Discussion

Two of the control lungs in figure 3 display clear ventilation heterogeneity as parts of the lungs remain dark in the hp ^{83}Kr MR images. The cause of the heterogeneity is unknown but the lungs were transported over a 3-h period, subsequent to excision, between the location of animal holding facility at Imperial College and the hp MRI facility at Nottingham. Nevertheless, the analysis of the SQUARE T_1 maps and histograms of all three control lungs led to comparable results with similar bimodal T_1 distribution. Figure 5 depicts the combined T_1 frequencies for the control group and for the elastase-treated animal lungs. The characteristic T_1 values from bimodal fitting are listed in table 2 and show little variation within the two groups (i.e. control and PPE group). The pronounced increase in the T_1^{EV} times for the PPE group in figure 5 and table 2 shows that the T_1^{EV} data can serve as an indicator for the development of the symptoms in the emphysema model. Presumably, the T_1^{EV} data are correlated to MAA. This correlation is expected from previous work with model surfaces but requires further corroboration in future studies. In any case however, the FWHM(T_1) data are not associated with the MAA differences between the two groups. This view is further supported by the box diagrams in figure 7, which show no overlap in T_1^{EV} data between the two groups. However, the associated FWHM(T_1) data almost completely overlap and are therefore unlikely to be useful as a biomarker for changes in MAA associated with the disease model.

Figure 7 also provides the results of statistical significance testing using Student's t-test at a critical significance level of

$\alpha = 0.05$. The null hypothesis, i.e. assuming no statistically significant difference in T_1^{EV} values between control and PPE group, was rejected for $T_1^{EV(f)}$ and $T_1^{EV(sl)}$ but not for FWHM($T_1^{(f)}$) and FWHM($T_1^{(sl)}$). This suggests that two parameters, namely $T_1^{EV(f)}$ and $T_1^{EV(sl)}$, are useful biomarkers for the elastase model of emphysema and may be sensitive to the increase in MAA.

A correlation between MAA and SQUARE would be caused by the dependence on lung S/V ratio. A decreasing S/V is expected from increasing MAA in the emphysema model [21,26] and it is known from previous work with model surfaces [3] that $T_1 \propto V/S$. In this work, the T_1 increase was not quantitatively correlated with the increase in MAA but a statistically significant increase in $T_1^{EV(f)}$ and $T_1^{EV(sl)}$ was observed for the emphysema model with increased MAA in histology compared with the control group. The bimodal appearance of the histogram could be caused by the presence of high S/V in the alveolar region and lower S/V within the airways. The alveoli may cause the fast relaxing mode described by $T_1^{EV(f)}$ with a narrow FWHM($T_1^{(f)}$) as the alveolar region will be fairly homogeneous. The airways, on the other hand, may contribute to the slow $T_1^{EV(sl)}$ mode with a broad distribution and hence a larger FWHM($T_1^{(sl)}$) due to the higher variability in S/V within the various airway generations. Note the relative contribution (in pixel count) between the two modes may not be quantitative due to the different extent of depolarization during the initial 0.2 s (fixed) delay and image acquisition. If the slow mode is indeed (at least partially) caused by the airways, the increase in $T_1^{EV(sl)}$ in the elastase-treated rat lungs would suggest that the S/V in the airways is affected by the disease model. Although this point was not further investigated, nitrogen chaser hp ^{83}Kr MRI could be used for future exploration where the airways are largely purged with a small volume of N$_2$ at the end of the inhalation [42].

The fifth lung (EL.5) from the PPE-treated group was excluded from the statistical analysis because the MAA increase developed asymmetrically in the left lung lobe only,
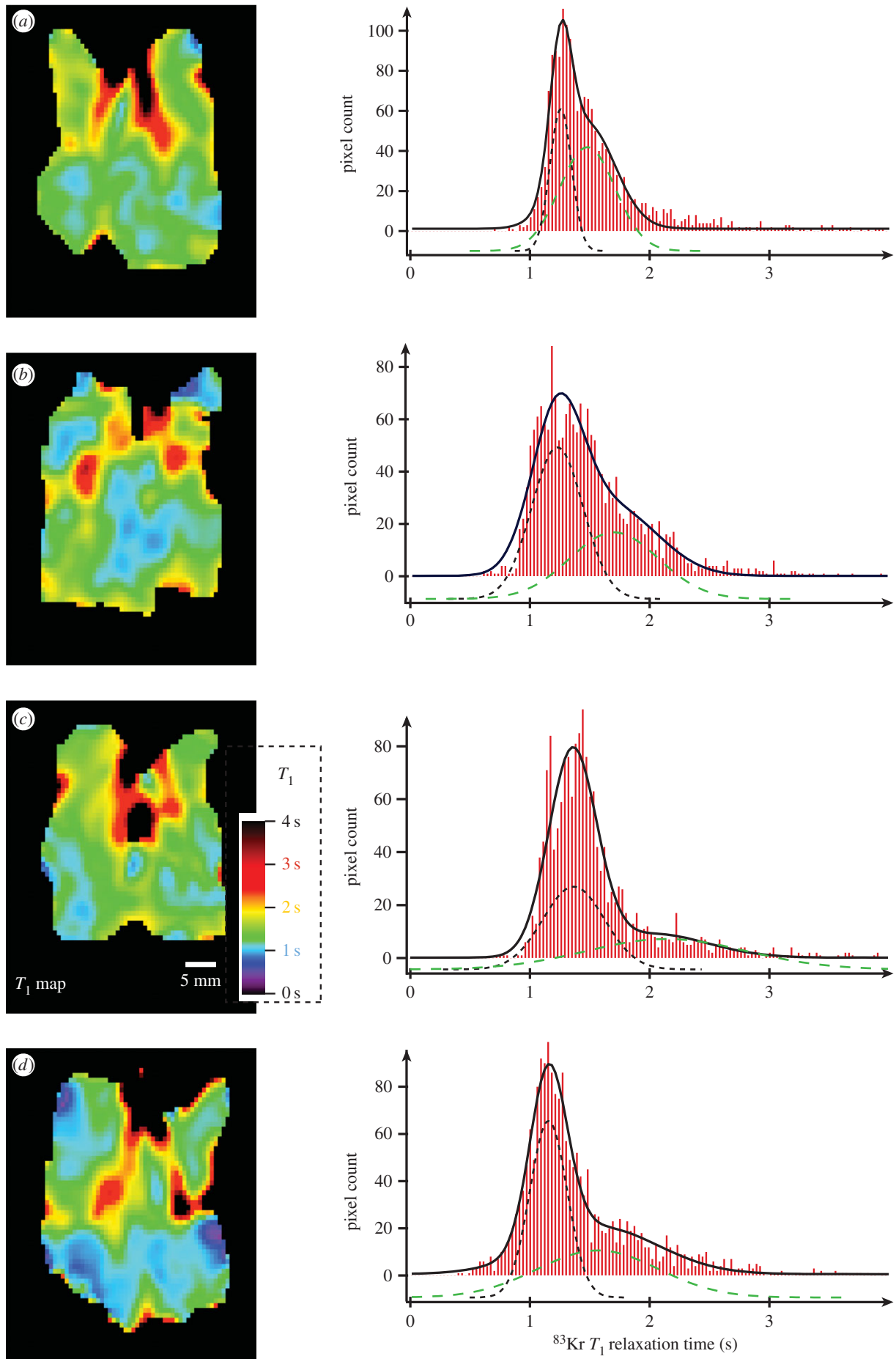
Figure 4. ^{83}Kr MRI T_1 maps (SQUARE contrast) of four of five PPE-treated lungs and their corresponding histograms. Green colours have now become more prevalent in the alveolar regions indicating increased T_1 values compared with those shown in figure 3. The histograms display the shift to larger T_1 values with $T_1^{EV(f)} \approx 1.3$ s (black dotted line), $T_1^{EV(f)} \approx 1.7$ s (green dashed line) with exact data listed in table 2. (a) Lung EL.1, (b) EL.2, (c) EL.3 and (d) EL.4. As in figure 3, the fast relaxing group has a narrower distribution than the slower relaxing group.
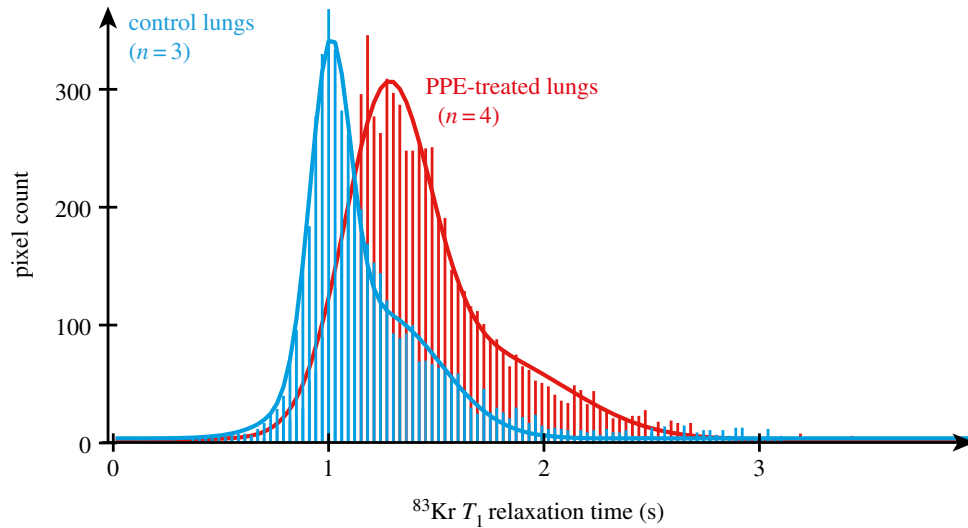
Figure 5. Histogram of all added T_1 frequencies. Data were obtained from the three control lungs (blue) in figures 3 and 4 elastase (PPE—red) treated animals (figure 4). The characteristic T_1 data from bimodal fitting (as in figures 3 and 4) are listed in table 2 and are very similar to the averaged characteristic T_1 values for control and elastase group. The sum of the bimodal fitting resulted to the blue solid line for the control group and the red solid line for the PPE group.
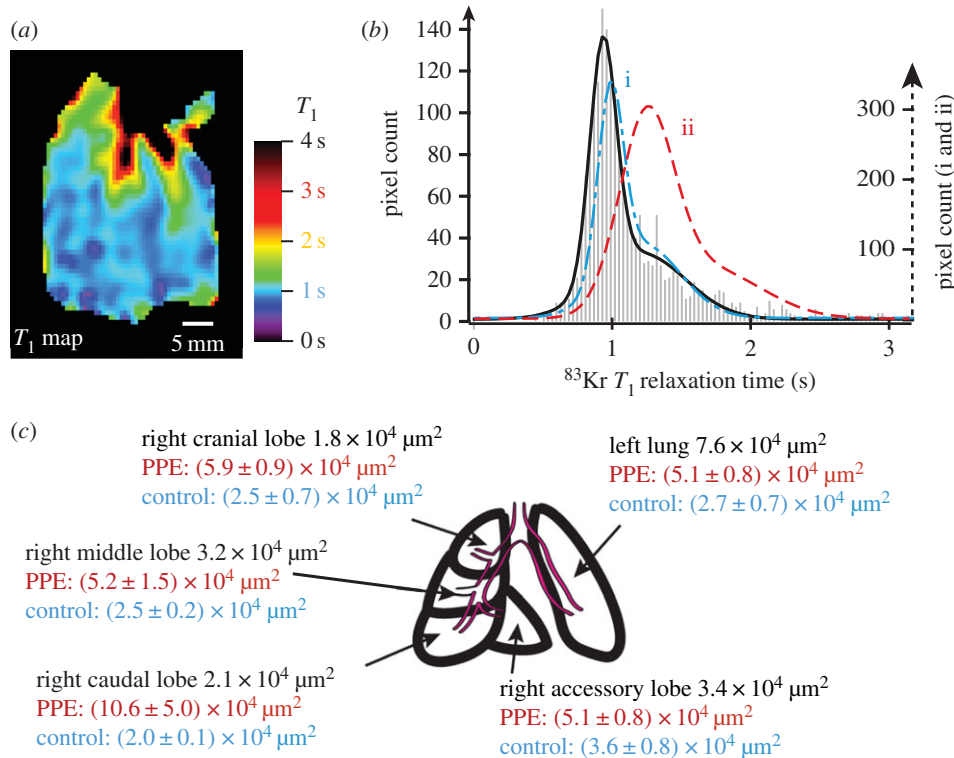

Figure 6. ^{83}Kr MRI T_1 maps (SQUARE contrast) of the PPE-treated lung EL.5 (a) and its corresponding histogram (b) with comparison of lobar mean alveolar area values (c). The grey bars indicate the experimental frequency of T_1 values and the solid black line is the combined result from bimodal fitting (the two individual components not shown but characteristic times listed in table 2). For comparison the outline of the resulting histogram from figure 5 is shown for the control group (blue dash–dotted line—i) and the elastase group (red dashed line—ii). Both the appearance of the SQUARE contrast and the histogram demonstrate that this lung has similar ^{83}Kr T_1 values to those lungs in the control group. (c) The mean alveolar area from lobar histology of PPE-treated lung EL.5 after the MRI experiments (black numbers) suggest that the emphysema model did not develop in all but the left lobe when compared with the mean values for the control (blue text—average from four control lungs) and PPE-treated groups (red text—average from six PPE lungs).

possibly owing to localized elastase deposition. From the data in figure 6c one would expect T_1 values similar to those from control lungs in all lobes except for the left lung lobe that exhibited very high MAA values. The SQUARE T_1 map and the corresponding histogram are indeed very similar to that of the control lungs, however, this also includes the T_1 values found in the left lobe. One would expect that the unexposed part of the lung to shows control lung behaviour, as indeed observed, but one would also expect very long T_1

times from the left lobe. However, the left lobe may have been damaged too excessively and some regions may, therefore, no longer be ventilated. These areas will not be able to contribute to the SQUARE T_1 map. Although non-ventilated areas should appear as 'dark' regions in the hp ^{83}Kr MR images, these zones may be masked by MR signals from unaffected regions that contribute to the non-slice selective images.

For this work, excised lungs have been used. Two of the control lungs exhibited ventilation defects that may have been
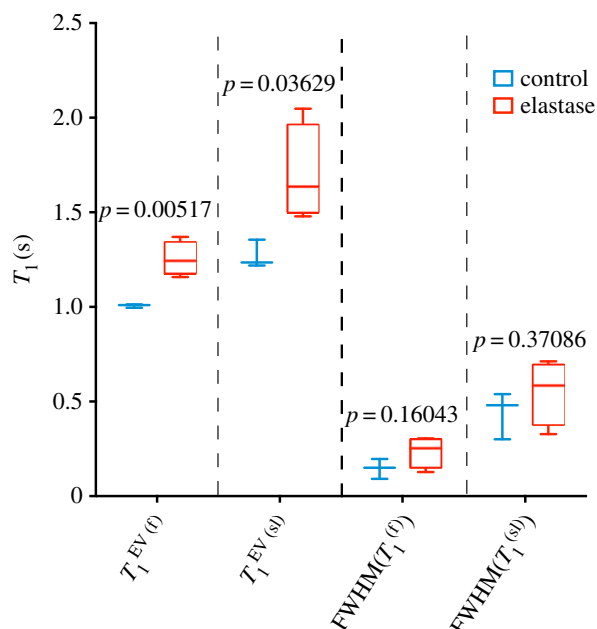
Figure 7. Box diagram of the characteristic data listed in table 2. The MRI $T_1^{EV(f)}$ data between control and elastase (PPE) group do not overlap. The same observation is made for the $T_1^{EV(sl)}$ data. In contrast, the distribution of T_1 values for the two modes of a histogram (characterized by FWHM(T_1)) significantly overlaps between control and PPE group, indicating that no significant statistical difference to be expected from the T_1 spread. However, the variation in T_1^{EV}, in particular $T_1^{EV(sl)}$, between the individual animals is more pronounced in the PPE group than in the control animals as visible in the added data in figure 5.

caused by the excision procedure and long transport period between the laboratories. Although this situation is non-ideal, the experiments demonstrate that the SQUARE T_1 contrast was little affected by any damage arising from lung excision, *ex vivo* transport, and *ex vivo* experiments. The MAA, obtained after MR image acquisition, were in the expected range for PPE and control group, except for EL.5 as discussed above.

This work demonstrated that hp ^{83}Kr SQUARE can serve as a biomarker for the elastase model of emphysema, in all likelihood because SQUARE senses changes in S/V. If the absence of harmful X-ray radiation is a strong motivation to explore the various pulmonary MRI techniques, a further potential advantage arises with hp ^{83}Kr: the SQUARE effect can be used as a pulmonary biomarker without the presence of pulsed magnetic field gradients (PFGs). Unlike ADC measurements where PFGs are required to generate the MRI contrast, SQUARE is solely caused by a relaxation rooted physical effect. Although PFGs are still needed for the MR image generation, hp ^{83}Kr SQUARE may have a potential as a global lung surface biomarker for pulmonary screening

without spatial resolution. Since the effect of relaxation can be measured remotely [37], SQUARE may be observed without an MRI scanner if the effect is remotely detected upon exhalation into a small bench-top NMR device.

The study presented here was focused on providing a first demonstration of hp ^{83}Kr SQUARE usage as an MRI contrast and biomarker for pulmonary pathophysiology in an animal model. Remarkably, using completely different physical concepts from those described here, krypton gas usage has been previously reported for contrast generation in dual energy computed tomography (DECT) [52]. The high-volume inhalation of a mixture of 80% krypton and 20% O_2 did not lead to adverse effects in COPD patients. Compared with CT, SQUARE MRI is expected to require lower krypton quantities for usable contrast generation. Finally, molecular oxygen does not dramatically accelerate ^{83}Kr T_1 relaxation and SQUARE measurements in rodent lungs [42] were unaffected by the presence of up to 40% O_2.

5. Conclusion

Informed by the previous S/V dependence of SQUARE in model surfaces, the aim of this work was to demonstrate the ability of hp ^{83}Kr SQUARE MRI to serve as a biomarker for the elastase model of emphysema. It was demonstrated that two characteristic T_1^{EV} times, obtained from bimodal fitting of the histograms, enable statistically significant distinction between emphysema model and control lung. Beyond statistics, the difference between the control group and emphysema model can also be identified from visual inspection of the ^{83}Kr SQUARE images shown in figures 3 and 4. The use of the simpler *ex vivo* model has allowed for rapid confirmation of the imaging technique despite some ventilation defects in the control group. Hp ^{83}Kr SQUARE may serve as a potential biomarker for pulmonary disease-related S/V ratio changes. Future quantification of the effect and comparison with other hp noble gas modalities will provide further evaluation of this technique. Because neither the application of magnetic field gradients nor the detection within high magnetic fields is required for SQUARE measurements, this new biomarker should also be explored for potential pulmonary mass screening using small bench-top devices.

References

1. Pavlovskaya GE, Cleveland ZI, Stupic KF, Meersmann T. 2005 Hyperpolarized krypton-83 as a new contrast agent for magnetic resonance imaging. *Proc. Natl Acad. Sci. USA* **102**, 18 275–18 279. (doi:10.1073/pnas.0509419102)

2. Cleveland ZI, Stupic KF, Pavlovskaya GE, Repine JE, Wooten JB, Meersmann T. 2007 Hyperpolarized Kr-83 and Xe-129 NMR relaxation measurements of hydrated surfaces: implications for materials science and pulmonary diagnostics. *J. Am. Chem. Soc.* **129**, 1784–1792. (doi:10.1021/ja065994t)

3. Stupic KF, Cleveland ZI, Pavlovskaya GE, Meersmann T. 2006 Quadrupolar relaxation of hyperpolarized krypton-83 as a probe for surfaces. *Solid State Nucl. Magn. Reson.* **29**, 79–84. (doi:10.1016/j.ssnmr.2005.08.008)

4. Six JS *et al.* 2014 Pulmonary MRI contrast using surface quadrupolar relaxation (SQUARE) of hyperpolarized Kr-83. *Magn. Reson. Imaging* **32**, 48–53. (doi:10.1016/j.mri.2013.08.007)

5. WHO. 2011 *World Health Statistics 2011*.

6. Mannino DM, Buist AS. 2007 Global burden of COPD: risk factors, prevalence, and future trends. *Lancet* **370**, 765–773. (doi:10.1016/S0140-6736(07)61380-4)

7. Vestbo J *et al*. 2008 Evaluation of COPD longitudinally to identify predictive surrogate end-points (ECLIPSE). *Eur. Respir. J.* **31**, 869–873. (doi:10.1183/09031936.00111707)

8. Han MK *et al*. 2010 Chronic obstructive pulmonary disease phenotypes the future of COPD. *Am. J. Resp. Crit. Care* **182**, 598–604. (doi:10.1164/rccm.200912-1843CC)

9. Litmanovich D, Boiselle PM, Bankier AA. 2009 CT of pulmonary emphysema—current status, challenges, and future directions. *Eur. Radiol.* **19**, 537–551. (doi:10.1007/s00330-008-1186-4)

10. Ley-Zaporozhan J, Ley S, Kauczor HU. 2008 Morphological and functional imaging in COPD with CT and MRI: present and future. *Eur. Radiol.* **18**, 510–521. (doi:10.1007/s00330-007-0772-1)

11. Fain S, Schiebler ML, McCormack DG, Parraga G. 2010 Imaging of lung function using hyperpolarized helium-3 magnetic resonance imaging: review of current and emerging translational methods and applications. *J. Magn. Reson. Imaging* **32**, 1398–1408. (doi:10.1002/jmri.22375)

12. Liu ZY, Araki T, Okajima Y, Albert M, Hatabu H. 2014 Pulmonary hyperpolarized noble gas MRI: recent advances and perspectives in clinical application. *Eur. J. Radiol.* **83**, 1282–1291. (doi:10.1016/j.ejrad.2014.04.014)

13. Mugler JP, Altes TA. 2013 Hyperpolarized ^{129}Xe MRI of the human lung. *J. Magn. Reson. Imaging* **37**, 313–331. (doi:10.1002/jmri.23844)

14. Lilburn DML, Hughes-Riley T, Six JS, Stupic KF, Shaw DE, Pavlovskaya GE, Meersmann T. 2013 Validating excised rodent lungs for functional hyperpolarized xenon-129 MRI. *PLoS ONE* **8**, e73468. (doi:10.1371/journal.pone.0073468)

15. Marshall H *et al*. 2012 Direct visualisation of collateral ventilation in COPD with hyperpolarised gas MRI. *Thorax* **67**, 613–617. (doi:10.1136/thoraxjnl-2011-200864)

16. Salerno M, de Lange EE, Altes TA, Truwit JD, Brookeman JR, Mugler JP. 2002 Emphysema: hyperpolarized helium 3 diffusion MR imaging of the lungs compared with spirometric indexes—initial experience. *Radiology* **222**, 252–260. (doi:10.1148/radiol.2221001834)

17. Yablonskiy DA, Sukstanskii AL, Leawoods JC, Gierada DS, Bretthorst GL, Lefrak SS, Cooper JD, Conradi MS. 2002 Quantitative *in vivo* assessment of lung microstructure at the alveolar level with hyperpolarized He-3 diffusion MRI. *Proc. Natl Acad. Sci. USA* **99**, 3111–3116. (doi:10.1073/pnas.052594699)

18. Woods JC *et al*. 2006 Hyperpolarized He-3 diffusion MRI and histology in pulmonary emphysema. *Magn. Reson. Med.* **56**, 1293–1300. (doi:10.1002/mrm.21076)

19. Sukstanskii AL, Yablonskiy DA. 2008 *In vivo* lung morphometry with hyperpolarized He-3 diffusion MRI: theoretical background. *J. Magn. Reson.* **190**, 200–210. (doi:10.1016/j.jmr.2007.10.015)

20. Yablonskiy DA, Sukstanskii AL, Woods JC, Gierada DS, Quirk JD, Hogg JC, Cooper JD, Conradi MS. 2009 Quantification of lung microstructure with hyperpolarized He-3 diffusion MRI. *J. Appl. Physiol.* **107**, 1258–1265. (doi:10.1152/japplphysiol.00386.2009)

21. Stephen MJ *et al*. 2010 Quantitative assessment of lung ventilation and microstructure in an animal model of idiopathic pulmonary fibrosis using hyperpolarized gas MRI. *Acad. Radiol.* **17**, 1433–1443. (doi:10.1016/J.Acra.2010.06.019)

22. Kaushik SS *et al*. 2011 Diffusion-weighted hyperpolarized ^{129}Xe MRI in healthy volunteers and subjects with chronic obstructive pulmonary disease. *Magn. Reson. Med.* **65**, 1154–1165. (doi:10.1002/mrm.22697)

23. Dregely I *et al*. 2011 Hyperpolarized xenon-129 gas-exchange imaging of lung microstructure: first case studies in subjects with obstructive lung disease. *J. Magn. Reson. Imaging* **33**, 1052–1062. (doi:10.1002/jmri.22533)

24. Kirby M *et al*. 2013 Pulmonary ventilation visualized using hyperpolarized helium-3 and xenon-129 magnetic resonance imaging: differences in COPD and relationship to emphysema. *J. Appl. Physiol.* **114**, 707–715. (doi:10.1152/japplphysiol.01206.2012)

25. Spector ZZ *et al*. 2005 Quantitative assessment of emphysema using hyperpolarized He-3 magnetic resonance imaging. *Magn. Reson. Med.* **53**, 1341–1346. (doi:10.1002/mrm.20514)

26. Emami K *et al*. 2008 Early changes of lung function and structure in an elastase model of emphysema—a hyperpolarized He-3 MRI study. *J. Appl. Physiol.* **104**, 773–786. (doi:10.1152/japplphysiol.00482.2007)

27. Ruppert K, Mata JF, Brookeman JR, Hagspiel KD, Mugler JP. 2004 Exploring lung function with hyperpolarized Xe-129 nuclear magnetic resonance. *Magn. Reson. Med.* **51**, 676–687. (doi:10.1002/mrm.10736)

28. Ruppert K, Mata JF, Wang HTJ, Tobias WA, Cates GD, Brookeman JR, Hagspiel KD, Mugler JP. 2007 XTC MRI: sensitivity improvement through parameter optimization. *Magn. Reson. Med.* **57**, 1099–1109. (doi:10.1002/mrm.21241)

29. Patz S *et al*. 2007 Hyperpolarized Xe-129 MRI: a viable functional lung imaging modality? *Eur. J. Radiol.* **64**, 335–344. (doi:10.1016/j.ejrad.2007.08.008)

30. Hersman FW *et al*. 2008 Large production system for hyperpolarized Xe-129 for human lung imaging studies. *Acad. Radiol.* **15**, 683–692. (doi:10.1016/j.acra.2007.09.020)

31. Driehuys B, Cofer GP, Pollaro J, Mackel JB, Hedlund LW, Johnson GA. 2006 Imaging alveolar-capillary gas transfer using hyperpolarized Xe-129 MRI. *Proc. Natl Acad. Sci. USA* **103**, 18 278–18 283. (doi:10.1073/pnas.0608458103)

32. Patz S *et al*. 2008 Human pulmonary imaging and spectroscopy with hyperpolarized Xe-129 at 0.2T. *Acad. Radiol.* **15**, 713–727. (doi:10.1016/j.acra.2008.01.008)

33. Patz S, Muradyan I, Hrovat MI, Dabaghyan M, Washko GR, Hatabu H, Butler JP. 2011 Diffusion of hyperpolarized ^{129}Xe in the lung: a simplified model of ^{129}Xe septal uptake and experimental results. *New J. Phys.* **13**, 015009. (doi:10.1088/1367-2630/13/1/015009)

34. Pavlovskaya G, Blue AK, Gibbs SJ, Haake M, Cros F, Malier L, Meersmann T. 1999 Xenon-131 surface sensitive imaging of aerogels in liquid xenon near the critical point. *J. Magn. Reson.* **137**, 258–264. (doi:10.1006/jmre.1998.1688)

35. Meersmann T, Deschamps M, Bodenhausen G. 2001 Probing aerogels by multiple quantum filtered Xe-131 NMR spectroscopy. *J. Am. Chem. Soc.* **123**, 941–945. (doi:10.1021/ja002747v)

36. Cleveland ZI, Pavlovskaya GE, Stupic KF, Wooten JB, Repine JE, Meersmann T. 2008 Detection of tobacco smoke deposition by hyperpolarized krypton-83 MRI. *Magn. Reson. Imaging* **26**, 270–278. (doi:10.1016/j.mri.2007.06.009)

37. Cleveland ZI, Pavlovskaya GE, Stupic KF, LeNoir CF, Meersmann T. 2006 Exploring hyperpolarized ^{83}Kr by remotely detected NMR relaxometry. *J. Chem. Phys.* **124**, 044312. (doi:10.1063/1.2159493)

38. Kuhn C, Tavassoli F. 1976 Scanning electron-microscopy of elastase-induced emphysema—comparison with emphysema in man. *Lab. Invest.* **34**, 2–9.

39. Snider GL, Lucey EC, Stone PJ. 1986 Animal models of emphysema. *Am. Rev. Respir. Dis.* **133**, 149–169.

40. Birrell MA, Wong S, Hele DJ, McCluskie K, Hardaker E, Belvisi MG. 2005 Steroid-resistant inflammation in a rat model of chronic obstructive pulmonary disease is associated with a lack of nuclear factor-κB pathway activation. *Am. J. Resp. Crit. Care* **172**, 74–84. (doi:10.1164/rccm.200409-1257OC)

41. Stevenson CS, Birrell MA. 2011 Moving towards a new generation of animal models for asthma and COPD with improved clinical relevance. *Pharmacol. Therapeut.* **130**, 93–105. (doi:10.1016/j.pharmthera.2010.10.008)

42. Stupic KF, Elkins ND, Pavlovskaya GE, Repine JE, Meersmann T. 2011 Effects of pulmonary inhalation on hyperpolarized krypton-83 magnetic resonance T-1 relaxation. *Phys. Med. Biol.* **56**, 3731–3748. (doi:10.1088/0031-9155/56/13/001)

43. Six JS, Hughes-Riley T, Stupic KF, Pavlovskaya GE, Meersmann T. 2012 Pathway to cryogen free production of hyperpolarized krypton-83 and xenon-129. *PLos ONE* **7**, e2997. (doi:10.1371/journal.pone.0049927)

44. Hughes-Riley T, Six JS, Lilburn DM, Stupic KF, Dorkes AC, Shaw DE, Pavlovskaya GE, Meersmann T. 2013 Cryogenics free production of hyperpolarized Xe and Kr for biomedical MRI applications. *J. Magn. Reson.* **237C**, 23–33. (doi:10.1016/j.jmr.2013.09.008)

45. Stupic KF, Cleveland ZI, Pavlovskaya GE, Meersmann T. 2011 Hyperpolarized Xe-131 NMR spectroscopy. *J. Magn. Reson.* **208**, 58–69. (doi:10.1016/J.Jmr.2010.10.004)

46. Frazer DG, Weber KC. 1976 Trapped air in ventilated excised rat lungs. *J. Appl. Physiol.* **40**, 915 – 922.

47. Hughes JMB, Rosenzweig DY. 1970 Factors affecting trapped gas volume in perfused dog lungs. *J. Appl. Physiol.* **29**, 332 – 339.

48. Zhao L, Mulkern R, Tseng CH, Williamson D, Patz S, Kraft R, Walsworth RL, Jolesz FA, Albert MS. 1996 Gradient-echo imaging considerations for hyperpolarized Xe-129 MR. *J. Magn. Reson. B* **113**, 179 – 183. (doi:10.1006/jmrb.1996.0173)

49. Birrell MA, Wong S, Hardaker EL, Catley MC, McCluskie K, Collins M, Haj-Yahia S, Belvisi MG. 2006 IκB kinase-2-independent and -dependent inflammation in airway disease models: relevance of IKK-2 inhibition to the clinic. *Mol. Pharmacol.* **69**, 1791 – 1800. (doi:10.1124/mol.105.019521)

50. Belloni PN, Garvin L, Mao CP, Bailey-Healy I, Leaffer D. 2000 Effects of all-trans-retinoic acid in promoting alveolar repair. *Chest* **117**, 235S – 241S. (doi:10.1378/chest.117.5_suppl_1.235S)

51. Cleveland ZI, Meersmann T. 2008 Density-independent contributions to longitudinal relaxation in Kr-83. *Chemphyschem* **9**, 1375 – 1379. (doi:10.1002/cphc.200800134)

52. Hachulla AL *et al*. 2012 Krypton ventilation imaging using dual-energy CT in chronic obstructive pulmonary disease patients: initial experience. *Radiology* **263**, 253 – 259. (doi:10.1148/Radiol.12111211)